

Epitaxy of ultrathin Fe_3O_4 films on $\text{SrTiO}_3(001)$: influence of growth parameters on the formation of coexisting (111)- and (001)-oriented phases

Andreas Alexander,^{a*} Kevin Ruwisch,^a Jannis Thien,^a Alexander Weissbach,^a Tobias Pollenske,^a Bin Zhang,^a Fabiola Schulte,^a Olof Gutowski,^b Alina Vlad,^c Alessandro Coati^c and Joachim Wollschläger^{a*}

Received 19 February 2026

Accepted 29 March 2026

Edited by J. Keckes, Montanuniversität Leoben, Austria

Keywords: magnetite; epitaxy; thin films; grazing-incidence X-ray diffraction; GIXRD; high-energy X-ray diffraction; HEXRD.

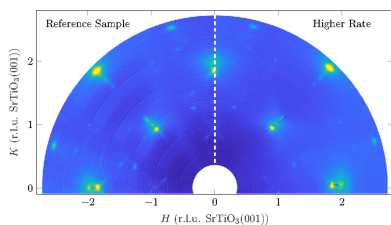
^aDepartment of Physics, Osnabrück University, Barbarastr. 7, 49076 Osnabrück, Germany, ^bDeutsches Elektronen-Synchrotron DESY, Notkestr. 85, 22607 Hamburg, Germany, and ^cSynchrotron SOLEIL, L'Orme des Merisiers, Départementale 128, 91190 Saint-Aubin, France. *Correspondence e-mail: aalexander@uni-osnabrueck.de, jwollsch@uni-osnabrueck.de

Ultrathin Fe_3O_4 films were grown on $\text{SrTiO}_3(001)$ substrates under systematically varied growth conditions (deposition rate and temperature, and film thickness) in order to determine the influence of these parameters on the formation of the coexisting (111) and (001) orientations of Fe_3O_4 . Structural characterization was performed using grazing-incidence X-ray diffraction and high-energy X-ray diffraction, including mapping of the reciprocal space in plane and out of plane to obtain detailed information about the structure of the films in the lateral and vertical directions. Despite an expected cube-on-cube growth, an intermediate layer of (111)-oriented Fe_3O_4 with hexagonal surface symmetry formed in all samples examined. This intermediate phase occurs in the form of 3D islands during the initial growth phase and persists even after growth has transformed to preferential formation of the (001) orientation. The fraction of the (111) phase, on the other hand, depends heavily on the kinetic conditions during growth. Its formation is favoured by low deposition rates and, above all, high deposition temperatures. These results support earlier observations and provide new insights into the structural development of Fe_3O_4 films on $\text{SrTiO}_3(001)$ in the early stages.

1. Introduction

Magnetite (Fe_3O_4) is of great interest as a candidate for applications in the fields of spintronics (Hoffmann & Bader, 2015; Hamie *et al.*, 2012; Seneor *et al.*, 1999; Kado, 2008; Wada *et al.*, 2010; Moussy, 2013) and spin caloritronics (Ramos *et al.*, 2016, 2013; Uchida *et al.*, 2016) due to a predicted 100% spin polarization at the Fermi level (Zhang & Satpathy, 1991). However, this promise has not met expectations, which might be due to interface effects (van der Zaag *et al.*, 2000; Jordan *et al.*, 2006; Marnitz *et al.*, 2015; Hu & Suzuki, 2002; Kado, 2008). For this reason, detailed knowledge of the growth of ultrathin magnetite films is necessary to control interface and surface properties required for high-quality spintronic devices (Moussy, 2013; Jordan *et al.*, 2006).

For the growth of magnetite ultrathin films, various substrates have been used, with $\text{MgO}(001)$ being the most widespread. Since its lattice constant results in a small mismatch of -0.3% between half the lattice constant of Fe_3O_4 and MgO , ordered pseudomorphic growth is given (Bertram *et al.*, 2013, 2012, 2011; Wollschläger, 2018; van der Zaag *et al.*, 2000; Chang *et al.*, 2016; Celotto *et al.*, 2003; Margulies *et al.*, 1997; Tobin *et al.*, 2007). However, growth and annealing of



OPEN ACCESS

Published under a CC BY 4.0 licence

Fe₃O₄ on MgO(001) substrates is limited in temperature, since above 250°C Mg²⁺ interdiffuses into the magnetite film (Wollschläger, 2018; Kim-Ngan *et al.*, 2009).

It has been demonstrated that interdiffusion of ferrite and SrTiO₃(001) substrates at elevated temperatures is prohibited (Rodewald *et al.*, 2019; Thien *et al.*, 2020). Therefore, despite a large lattice mismatch of 7.5% between the SrTiO₃ substrate and half the lattice constant of Fe₃O₄, magnetite films can also be grown on it, even at elevated temperatures (Kuschel *et al.*, 2016). Furthermore, due to the large lattice mismatch, the use of SrTiO₃(001) as a substrate offers the possibility of studying strain effects, which can be used to modify the electronic and magnetic properties of Fe₃O₄ (Kuschel *et al.*, 2016; Monti *et al.*, 2013; Kale *et al.*, 2001; Rubio-Zuazo *et al.*, 2015; Liu *et al.*, 2017; Chen *et al.*, 2008).

For the growth of Fe₃O₄ on SrTiO₃(001), cube-on-cube growth is expected and is also frequently observed (Kuschel *et al.*, 2017; Pohlmann *et al.*, 2022; Alexander *et al.*, 2025; Wollschläger, 2018). However, for high temperatures, *i.e.* $T \geq 700^\circ\text{C}$, Fe₃O₄ has been reported to grow in its (111) orientation with hexagonal surface symmetry (Takahashi *et al.*, 2012, 2014; Leung *et al.*, 2008). This effect is attributed to both the large lattice mismatch (7.5%) and the anisotropy of the surface energy of the spinel structure of Fe₃O₄, which leads to competition between (111) and (001) growth orientations (Mishra & Thomas, 1977; Yu *et al.*, 2012; Santos-Carballal *et al.*, 2014). In recent work, using surface-sensitive spot-profile-analysis low-energy electron diffraction (LEED) measurements, the (111) orientation of Fe₃O₄ on SrTiO₃(001) was observed at even lower temperatures (250°C) as an initial interface structure before it continues to grow in the (001) orientation with cubic surface structure (Alexander *et al.*, 2025).

In this work we analyse the conditions under which the (111) orientation of Fe₃O₄ is preferentially formed and their influence on the growth behaviour. In particular, the aim is to find out whether the (111) orientation is only a temporary intermediate phase that is transformed into the (001) orientation in the further growth of the thin film or whether this phase persists and coexists with the later (001) orientation.

For this reason, in this work, ultrathin magnetite films have been grown on SrTiO₃(001) by reactive molecular beam epitaxy (RMBE) and analysed *in situ* by means of synchrotron-radiation-based (grazing-incidence) X-ray diffraction (GIXRD) and high-energy X-ray diffraction (HEXRD), providing detailed structural information of the surface, interface and film structure. By varying the growth parameters, their influence on film growth and the formation of the (111) orientation of Fe₃O₄ was studied.

2. Experimental details

The magnetite thin films were prepared and *in situ* characterized at the SixS beamline of Synchrotron SOLEIL (Saint-Aubin, France). Here, the diffractometer is coupled to three ultra-high vacuum chambers with a base pressure of 2×10^{-10} mbar, enabling (grazing-incidence) X-ray diffrac-

tion experiments directly after film growth without breaking the vacuum (Dawiec *et al.*, 2016).

Before deposition, the SrTiO₃(001) substrates were cleaned by annealing for 90 min at 420°C in a molecular oxygen atmosphere of 5×10^{-5} mbar in order to remove adsorbates.

The films were grown by RMBE, *i.e.* thermal evaporation from a pure Fe target in a molecular oxygen atmosphere of 5×10^{-6} mbar. During deposition of the first film, the substrate temperature was kept at 420°C and a constant deposition rate was controlled by the flux of the evaporator. This procedure was used to calibrate the deposition rate as recorded by a quartz crystal microbalance prior to the experiments. Afterwards, further samples were prepared by varying one growth parameter at a time, *i.e.* deposition rate, film thickness and temperature (*cf.* Fig. 1). Thus, the influence on the growth behaviour of each parameter can be analysed separately.

For the following diffraction experiments, a photon energy of 16 keV was used and the data were collected by an XPAD S140 two-dimensional detector. In order to obtain information on the out-of-plane structure of the films, X-ray diffraction (XRD) was performed using the θ - 2θ geometry. Subsequently, using a grazing-incidence geometry (GIXRD) with a fixed glancing angle of 0.2°, scans along several crystal truncation rods (CTRs) attributed to Fe₃O₄(001) and Fe₃O₄(111) were performed. In the following, the two different Fe₃O₄ orientations, (001) and (111), are labelled ‘cub’ and ‘hex’, respectively, referring to the square and hexagonal surface structure, respectively. Moreover, two-dimensional in-plane mappings were recorded.

After transport under ambient conditions, films were additionally studied by means of HEXRD at the P07 beamline (EH2) of PETRA III at DESY. For the diffraction experiment, a photon energy of 73.3 keV and a glancing angle of $\theta = 0.03^\circ$ were used. The data were collected by a Varex XRD 4343 CT 2D area detector. During the measurement, the samples were rotated between $\pm 90^\circ$ with a rotation speed of 0.5° s^{-1} to collect the diffraction signal from the entire sample. Afterwards, the detector images of these scans were summed in order to obtain a full reciprocal-space map of the entire film.

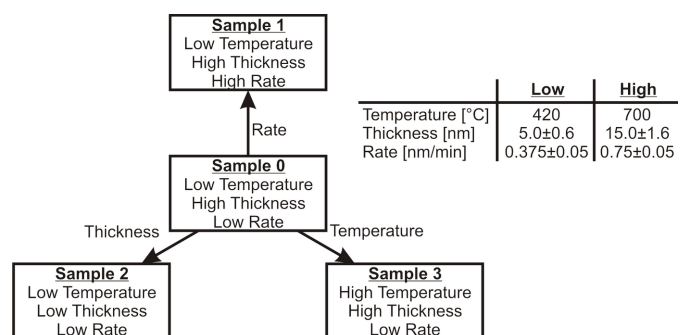


Figure 1 Scheme of studied samples including experimental parameters such as growth temperature, film thickness and deposition rate. First, sample 0 (S0) was analysed as a reference. Subsequently, only one parameter was varied at a time in order to analyse its influence on the structure.

3. Results

3.1. Reference sample S0

Fig. 2 shows an in-plane reciprocal-space map for low L values $\{0.02 < L < 0.1$ [r.l.u. (reciprocal-lattice units) SrTiO₃(001)]}. Besides the expected reflections of the SrTiO₃ substrate (green crosses) and reflections of the cubic (001) orientation of Fe₃O₄ (red squares), reflections with a 12-fold symmetry can be found. These are reflections of the hexagonal surface structure of Fe₃O₄(111), which is present in two domains, A (yellow circles) and B (yellow diamonds), rotated by 90°, as well as the respective mirror domains \bar{A} and \bar{B} . The latter two domains are not found in Fig. 2 as their in-plane reflections fully overlap with reflections from A and B . However, the mirror domains can be distinguished using higher out-of-plane scattering vectors (higher values of L).

Since $(20\bar{2})_{\text{hex}}^A$ coincides with $(220)_{\text{cub}}$ [close to $(110)_{\text{STO}}$], it is evident that the orientation of Fe₃O₄(111) with respect to the substrate is

$$\text{Fe}_3\text{O}_4[10\bar{1}](111)\|\text{SrTiO}_3[110](001) \text{ for domain } A$$

and

$$\text{Fe}_3\text{O}_4[10\bar{1}](111)\|\text{SrTiO}_3[\bar{1}10](001) \text{ for domain } B,$$

and analogously for their mirror domains \bar{A} and \bar{B} , respectively. A graphical representation of the orientation of Fe₃O₄(111) on the substrate is shown in Fig. 3. The 12-fold symmetry and the positions of the in-plane Fe₃O₄(111) reflections show that the Fe₃O₄(111) layer is (almost) fully relaxed. This result contradicts the model proposed by Takahashi *et al.* (2012), which suggests that the Fe₃O₄(111) film adapts to the lattice of the SrTiO₃(001) substrate in the sense

× SrTiO₃ ■ Fe₃O₄(001) ○ Fe₃O₄(111)_A ◇ Fe₃O₄(111)_B

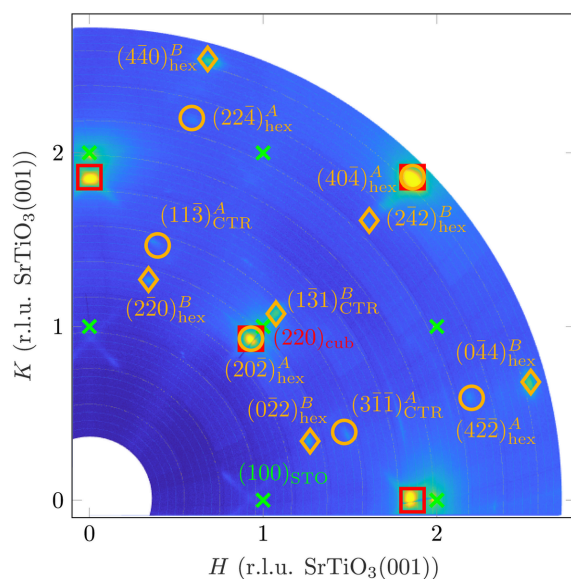


Figure 2

Section of an in-plane reciprocal-space map of reference sample for summation of intensities running the scaled out-of-plane scattering-vector magnitude L between 0.02 and 0.1 [r.l.u. SrTiO₃(001)]. For reasons of clarity, only reflections/CTRs that can be detected are included.

of a superstructure. This would lead to distorted diffraction patterns with a sixfold instead of a 12-fold symmetry.

The cross-shaped weak intensities around the Fe₃O₄(001) reflections indicate facets with an in-plane component in the $\langle 110 \rangle$ directions.

Since only the square surface structure of the Fe₃O₄(001) can be seen with surface-sensitive electron diffraction (LEED), here it can be concluded from the presence of the Fe₃O₄(111) reflections that the (111) orientation is not a temporary intermediate phase that transforms into the (001). Rather, a permanent Fe₃O₄(111) interlayer is stabilized at the interface that continues to coexist with the Fe₃O₄(001) film.

Fig. 4(a) presents a $(00L)$ XRD scan performed at the reference sample. Besides the expected reflections of the substrate, the $(004)_{\text{cub}}$ reflection can be seen due to (001)-oriented (majority) fractions of the Fe₃O₄ film. Near this Bragg peak, no Laue fringes are observed, pointing to an inhomogeneous crystalline order of Fe₃O₄(001).

Furthermore, the $(222)_{\text{hex}}$ reflection, expected at $L = 1.62$, is not present. Although the intensity of Fe₃O₄(222) is weak compared with Fe₃O₄(004) due to its structure factor, the complete absence of the reflection indicates that most of the Fe₃O₄ film grows with the (001) orientation.

The full width at half-maximum (FWHM) of $(004)_{\text{cub}}$ is used to determine the crystalline film thickness d_{cryst} according to the Scherrer formula (Scherrer, 1918):

$$d_{\text{cryst}} = K_S \frac{a_f}{\text{FWHM}}, \quad (1)$$

with $K_S = 0.89$ and a_f being the bulk lattice constant of Fe₃O₄. This results in a crystalline film thickness $d_{\text{cryst}} = 14.0$ (2) nm. A comparison with the deposited film thickness shows that d_{cryst} is only slightly lower, meaning that most of the layer is ordered crystalline.

Fig. 4(b) shows the diffractogram recorded for the $(22)_{\text{cub}}$ -CTR of Fe₃O₄(001). Fe₃O₄ reflections due to both Fe₃O₄(001) and Fe₃O₄(111) can lie on this CTR [cf. Fig. 4(c)]. Besides the two Fe₃O₄-related reflections $(222)_{\text{cub}}$ and $(224)_{\text{cub}}$

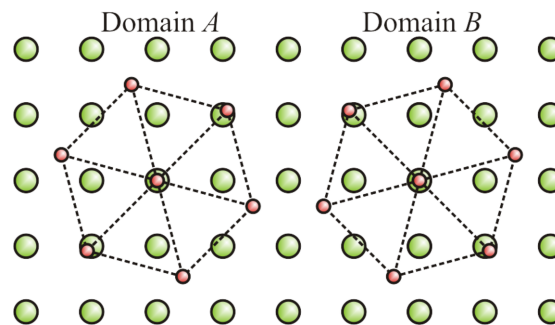


Figure 3

Schematic model for the in-plane orientation of Fe₃O₄(111) grown on SrTiO₃(001). The larger green circles denote the Sr²⁺ cations and the smaller red circles represent the Fe³⁺ cations of the Fe₃O₄(111) unit cell. For simplicity, Ti and O atoms are not shown and the surface unit cell of Fe₃O₄(111) is used. The two possible domains, A and B , rotated by 90°, are shown. [Adapted from Leung *et al.* (2008).]

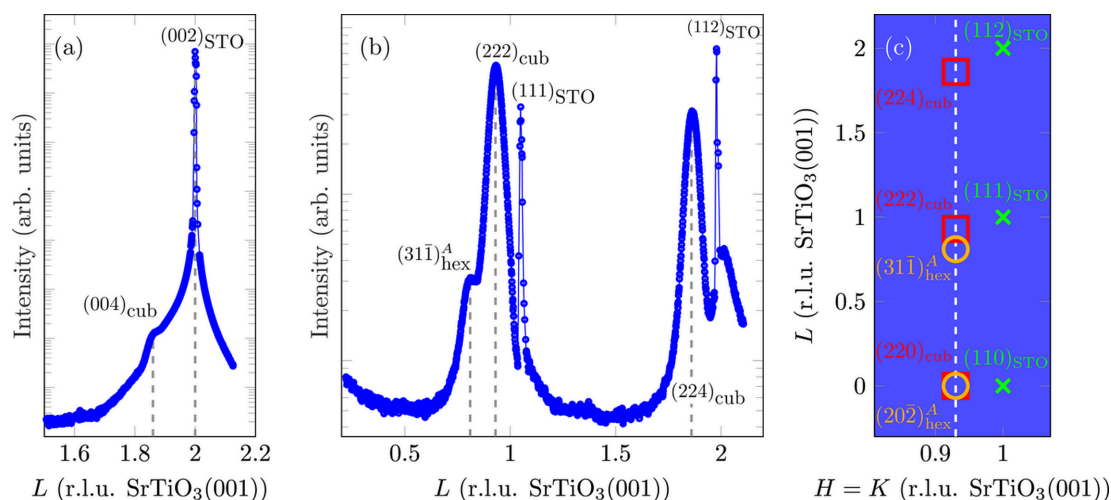


Figure 4
 (a) XRD scan along the (00)-CTR of the reference sample. Since nothing can be seen in the range $L < 1.5$ except for the substrate reflection, this is not shown. (b) L scan along the $(22)_{\text{cub}}$ -CTR of $\text{Fe}_3\text{O}_4(001)$ of the reference sample ($H \approx K \approx 0.93$, cf. Fig. 2). Here, the sharp outliers at $L = 1$ and $L = 2$ are due to diffuse scattering close to very intense substrate Bragg peaks being close to the measured Fe_3O_4 CTR. (c) Schematic sketch of the reflections expected on and near the $(22)_{\text{cub}}$ -CTR of completely relaxed $\text{Fe}_3\text{O}_4(001)$ and $\text{Fe}_3\text{O}_4(111)$.

at $L = 0.93$ and $L = 1.86$, respectively, an additional reflection is present at $L = 0.81$. This reflection is attributed to $(31\bar{1})_{\text{hex}}^A$ of $\text{Fe}_3\text{O}_4(111)$.

The intensities of $(222)_{\text{cub}}$ and $(31\bar{1})_{\text{hex}}^A$ are used to determine the quantity of (111)-orientated Fe_3O_4 . For this, the structure factors F_{HKL} of the respective reflections must be taken into account. Structure factors were calculated from the spinel structure using atomic form factors from Brown *et al.* (2006). Consequently, the normalized intensity yield $Y_{\text{hex}/\text{cub}}$, i.e. the fraction of Fe_3O_4 with (111) orientation, can be calculated as

$$Y_{\text{hex}/\text{cub}} = \frac{I_{31\bar{1}}/|F_{31\bar{1}}|^2}{I_{31\bar{1}}/|F_{31\bar{1}}|^2 + I_{222}/|F_{222}|^2} = 0.77\%. \quad (2)$$

Only the $\text{Fe}_3\text{O}_4(111)$ reflections of one domain and its mirror domain (here, A and \bar{A}) are apparent at this position. Assuming a statistically uniform distribution of the domains, the overall fraction of Fe_3O_4 with (111) orientation is twice as high, i.e. 1.5%.

Taking this result and the respective structure factors into account, it is obvious that the $(222)_{\text{hex}}$ reflection, which would be expected at approximately $L = 1.62$ on the $(00L)$ CTR, is not visible in the XRD measurement [cf. Fig. 4(a)], as its intensity is only 0.3% of that of $(004)_{\text{cub}}$ and it therefore vanishes into the background. The same applies to $(111)_{\text{hex}}$, expected at $L = 0.81$.

From the vertical difference between the two reflections $(222)_{\text{cub}}$ and $(224)_{\text{cub}}$, a vertical lattice constant of $a_{\perp} = 839.2$ (10) pm can be determined. Within the experimental uncertainty, this is in good agreement with the value of 839.6 pm for bulk magnetite (Cornell & Schwertmann, 2003), demonstrating again complete relaxation of the $\text{Fe}_3\text{O}_4(001)$ film in the vertical direction. A detailed discussion will be presented later.

The FWHM analysis of the reflections shows that for $\text{Fe}_3\text{O}_4(001)$ there is a broadening of the FWHM with increasing scattering-vector magnitude q , which is nearly linear (cf. Fig. 5). This broadening with increasing scattering vector indicates mosaics, i.e. parts of the surface that are slightly tilted with respect to the $\text{SrTiO}_3(001)$ surface. In this case, the broadening of the spot profiles is related to the spread of the tilted mosaics, i.e. the sharpness of the distribution of mosaic angles, which is highly dependent on the lattice mismatch (Wollschläger *et al.*, 2001). The slope of the linear incline corresponds to the mosaic spread $\Delta\sigma$, while the

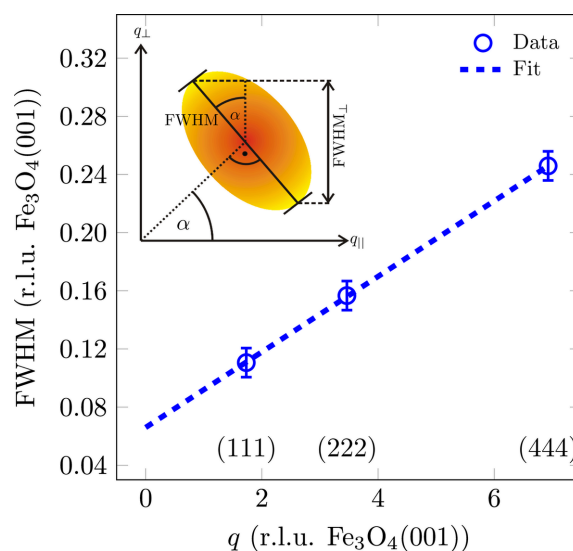


Figure 5
 FWHM analysis of (LLL) reflections of (001)-oriented Fe_3O_4 of the reference sample as a function of the scattering-vector magnitude q . The FWHM of the peaks has been fitted with a linear function. The inset shows the projection of the effective FWHM onto the measured vertical FWHM_{\perp} .

FWHM for the extrapolation $\lim_{q \rightarrow 0}$ is caused by finite size effects resulting from the size of the mosaics. These mosaics can be attributed to the formation of misfit dislocations at the interface for strain release caused by the lattice mismatch between $\text{Fe}_3\text{O}_4(001)$ and $\text{SrTiO}_3(001)$ as observed in different material systems with high lattice mismatch (Goldbach & Wollschläger, 2022; Wollschläger *et al.*, 2001; Dynna *et al.*, 1996; Vassent *et al.*, 1996). Since the broadening of the reflections is perpendicular to the origin or to the scattering vector \mathbf{q} but the L scan only measures the vertical component of the FWHM_\perp , a corresponding correction must be made for each measured FWHM_\perp in order to calculate the projection of the FWHM (*cf.* inset in Fig. 5).

A fitting of the FWHM with a linear function (*cf.* Fig. 5) results in a mosaic spread of $\Delta\sigma = 1.82(4)^\circ$ and a constant offset of 0.066 (r.l.u. Fe_3O_4) that corresponds to a lateral mosaic size of $d_{\text{mosaic}} = 11.3(2)$ nm with respect to the [111] direction.

3.2. Influence of deposition rate

The first variation in film growth parameters was a higher deposition rate, achieved by increasing the material flux of the evaporator. Therefore, the deposition rate was increased from 0.375 to 0.750 nm min^{-1} while keeping the deposition temperature and final film thickness constant. For the latter, the deposition time was halved.

Qualitatively, no significant difference can be seen in the in-plane maps with a change in the deposition rate (*cf.* Fig. 6). The reflections of the (111) orientation (white arrows) are slightly more pronounced at a lower deposition rate, especially the non-integer CTRs without in-plane reflections (red arrows). In addition, the crosses caused by facets on the $\text{Fe}_3\text{O}_4(001)$ reflections are slightly more pronounced, which indicates that the proportion of facets has increased, *i.e.* larger facets have been formed or more facets have been formed.

In the XRD measurements on the (00 L) rod with a higher deposition rate, there is also no significant difference from the reference sample [*cf.* Fig. 7(a)]. The (004)_{cub} reflection has a slightly higher intensity, so that it is more apparent.

The FWHM of (004)_{cub} gives a crystalline layer thickness of $d_{\text{cryst}} = 12.9(2)$ nm according to equation (1). Despite the initial deposited volume of Fe_3O_4 being the same, this is slightly lower than for the reference sample, which could be explained by the fact that the layer with the lower growth rate can arrange its structure better.

Equally on the (22)_{cub}-CTR, no significant qualitative difference can be seen between the two samples [*cf.* Fig. 7(b)]. The reflection $(31\bar{1})_{\text{hex}}^A$ belonging to the (111) orientation of Fe_3O_4 can also be seen for both preparations. Using the intensity ratio of (222)_{cub} and $(31\bar{1})_{\text{hex}}^A$ according to equation (2), the fraction of (111)-orientated Fe_3O_4 (both A and \bar{A} domains) in the sample with the higher deposition rate is 0.4%. This is a decrease by half compared with the reference sample, suggesting that a lower deposition rate favours the formation of the (111) orientation, and supports the qualitative observations from the comparison of the in-plane maps for the two preparations (*cf.* Fig. 6).

Fig. 8 shows the FWHM versus the scattering-vector magnitude q for the $\text{Fe}_3\text{O}_4(001)$ reflections. The sample with a higher deposition rate also shows a widening with q , which indicates tilting mosaics. For this reason, the FWHM was fitted with a linear function to determine the mosaic size d_{mosaic} and the mosaic spread $\Delta\sigma$. Similarly to the crystalline film thickness, the lateral mosaic size with respect to the [111] direction for the sample with a higher deposition rate is slightly lower at $d_{\text{mosaic}} = 10.3(2)$ nm than for the reference sample [$d_{\text{mosaic}} = 11.3(2)$ nm].

From the slope of the FWHM with q , a mosaic spread of $\Delta\sigma = 1.34(4)^\circ$ is obtained for the sample with a higher deposition rate. This is also slightly lower than that for the reference sample [$\Delta\sigma = 1.82(4)^\circ$], which indicates a sharper distribution of mosaic angles with a higher deposition rate.

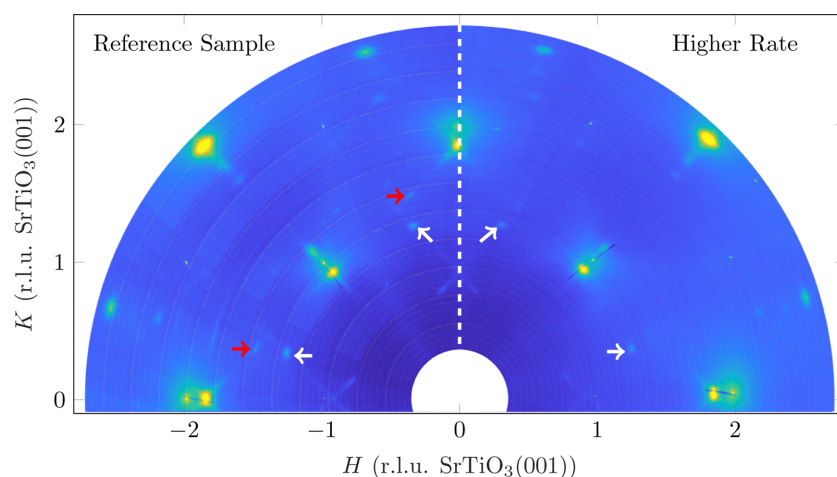


Figure 6

Comparison of the in-plane reciprocal-space maps of the reference sample (left) and the sample with higher deposition rate (right). The L value is a summation between 0.02 and 0.1 [r.l.u. $\text{SrTiO}_3(001)$] (*cf.* Fig. 2). The white arrows denote in-plane reflections of the (111) orientation, while the red arrows denote CTRs of the (111) orientation without in-plane reflections.

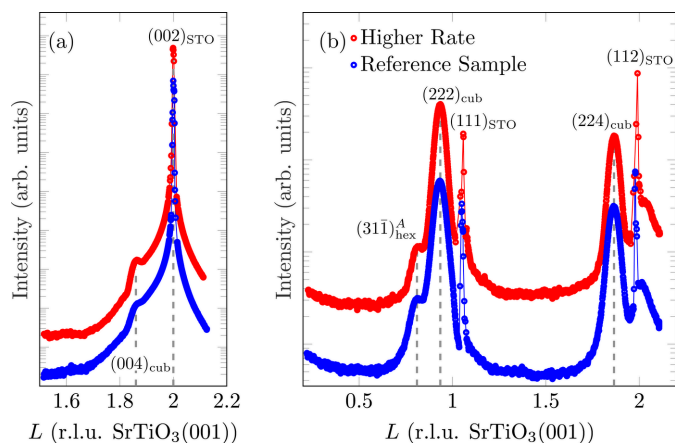


Figure 7
 (a) Comparison of XRD scans along the (00)-CTR for different deposition rates. (b) Comparison of L scans along the $(22)_{\text{cub}}$ -CTR of $\text{Fe}_3\text{O}_4(001)$ for different deposition rates. Here, the sharp outliers at $L = 1$ and $L = 2$ are due to diffuse scattering close to very intense substrate Bragg peaks being close to the measured CTRs.

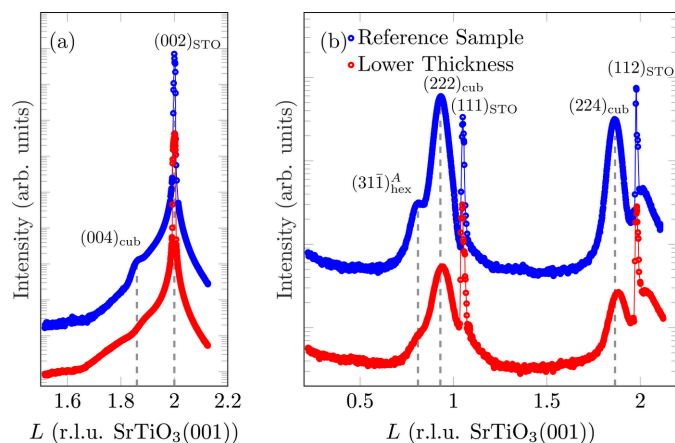


Figure 9
 (a) Comparison of XRD scans along the (00)-CTR for films of different thicknesses. (b) Comparison of L scans along the $(22)_{\text{cub}}$ -CTR of $\text{Fe}_3\text{O}_4(001)$ for different film thickness. Here, the sharp outliers at $L = 1$ and $L = 2$ are due to diffuse scattering close to very intense substrate Bragg peaks being close to the measured CTRs.

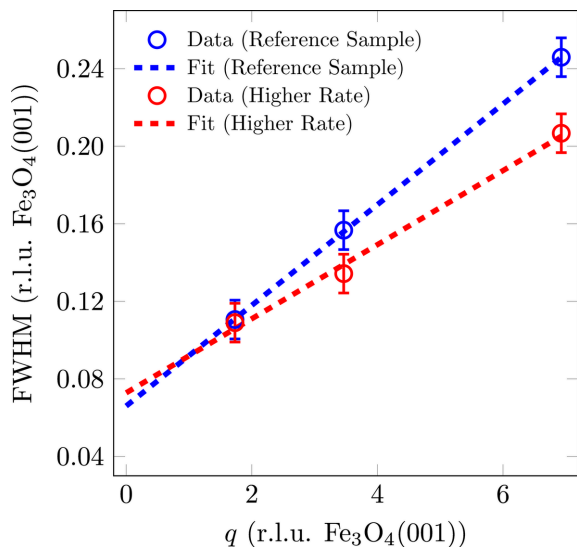


Figure 8
 FWHM analysis of (LLL) reflections of (001) -oriented Fe_3O_4 as a function of the scattering-vector magnitude q for different deposition rates. The FWHM of the peaks has been fitted with a linear function.

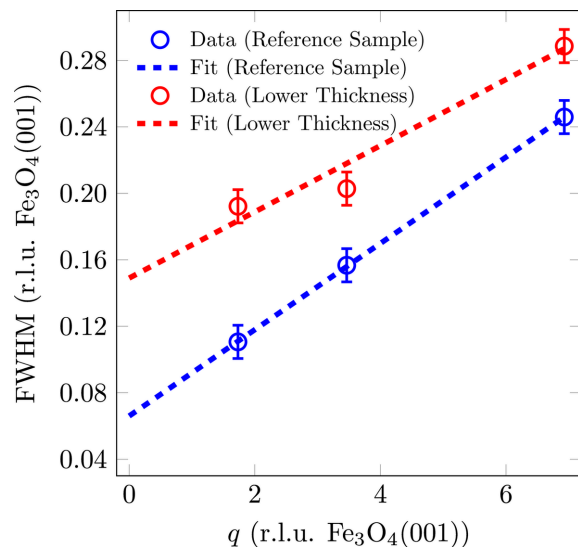


Figure 10
 FWHM analysis of (LLL) reflections of (001) -oriented Fe_3O_4 as a function of the scattering-vector magnitude q for different film thicknesses. The FWHM of the peaks has been fitted with a linear function.

3.3. Influence of film thickness

The second variation in film growth parameters was a lower film thickness d_f . To achieve this, the deposition time was reduced to one-third of that used for the reference sample while the deposition rate and temperature were kept constant.

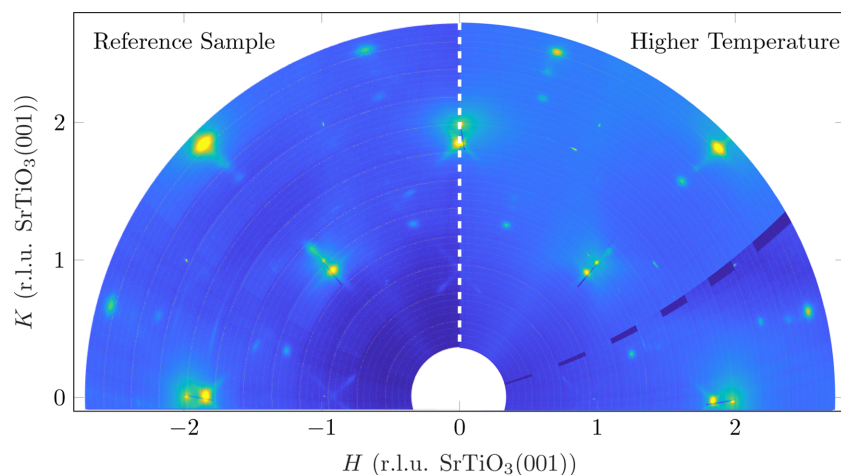
Because there was insufficient signal intensity from the magnetite film, no in-plane map could be recorded, while it was possible to record out-of-plane scans.

There are no significant qualitative differences either in the XRD measurement along the (00)-CTR or in the L scan along the $(22)_{\text{cub}}$ -CTR (cf. Fig. 9). The intensity of the reflections is evidently weaker in the thinner film, as expected due to the probed film volume. Since $(004)_{\text{cub}}$ could not be reasonably fitted due to its low intensity, it was not possible to determine

the crystalline layer thickness according to the Scherrer equation.

The intensity ratio between $(31\bar{1})_{\text{hex}}^A$ and $(222)_{\text{cub}}$ as obtained from the $(22)_{\text{cub}}$ -CTR of $\text{Fe}_3\text{O}_4(001)$ results in a fraction of (111) -oriented Fe_3O_4 of 1.95% according to equation (2). Compared with the reference sample, this is an increase in the proportion by a factor of 2.5 and corresponds very well to the respective reduction in film thickness. This means that the (111) orientation forms directly at the beginning of film growth and the Fe_3O_4 film then continues to grow exclusively in the (001) orientation. The (111) orientation is therefore present as a permanent intermediate layer.

The reflections of $\text{Fe}_3\text{O}_4(001)$ also broaden with increasing q for the sample with a lower layer thickness (cf. Fig. 10). The


Figure 11

Comparison of the in-plane reciprocal-space maps of the reference sample (left, deposition temperature 420°C) and the sample with increased deposition temperature (right, 700°C). The L value is a summation between 0.02 and 0.1 [r.l.u. SrTiO₃(001)]. The dark regions on the right-hand side are artefacts caused by the overlap of the individual detector images.

fit gives a lateral mosaic size with respect to the [111] direction of $d_{\text{mosaic}} = 5.0$ (2) nm and a mosaic spread of $\Delta\sigma = 1.36$ (4)°. Since the crystalline layer thickness d_{cryst} could not be determined using the XRD scan along the (00 L) rod, the projection of the mosaic size perpendicular to the substrate [$d_{\text{mosaic}}^{\text{vert}} = 4.2$ (2) nm] is used to estimate the crystalline film thickness. Accordingly, the crystalline layer thickness d_{cryst} must be in-between the vertical mosaic size $d_{\text{mosaic}}^{\text{vert}}$ and the evaporated film thickness d_{f} , i.e. $4.0 < d_{\text{cryst}} < 5.6$ nm.

The mosaic spread is lower than for the reference sample and indicates that the distribution of mosaic angles is sharper at the beginning of the growth and broadens with increasing film thickness.

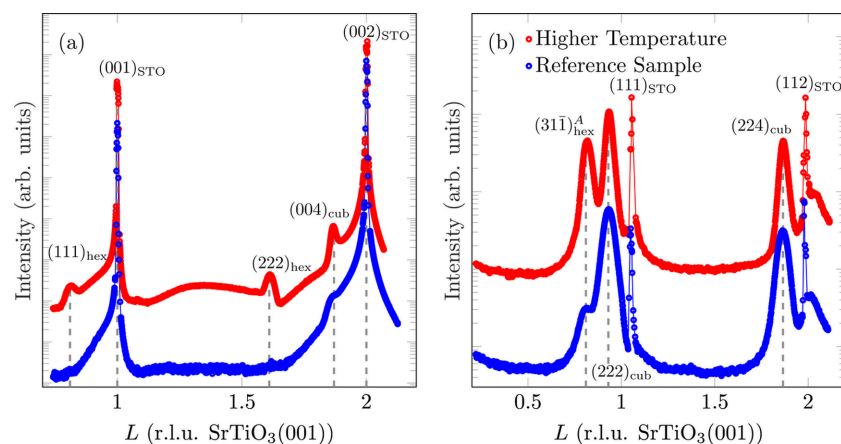
3.4. Influence of deposition temperature

The third variation in film growth parameters was a higher deposition temperature. The deposition temperature was

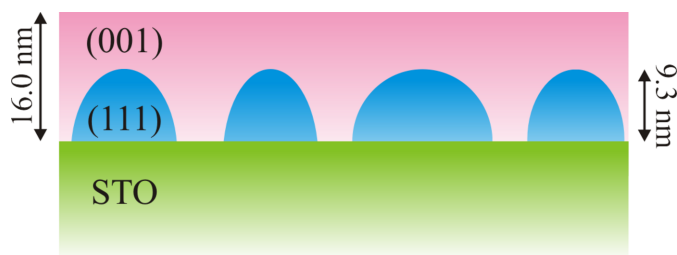
increased from 420 to 700°C, while the deposition rate and time (film thickness) were kept constant.

Fig. 11 shows the comparison of the reciprocal in-plane maps for deposition at different temperatures. All reflections of Fe₃O₄, from both (001) and (111) orientations, are significantly sharper and more pronounced in the sample that was grown at a higher temperature. This indicates higher crystalline order in the lateral direction for both orientations of Fe₃O₄. Furthermore, the cross-shaped weak intensities around the Fe₃O₄(001) reflections caused by facets can be seen here. Although these are sharper, they are less pronounced compared with those for the film deposited at lower temperature (reference sample).

In the XRD scan along the (00 L) rod [cf. Fig. 12(a)], the reflections of the (001) orientation of Fe₃O₄ are sharp and clearly pronounced, which indicates a high crystalline order. Furthermore, at $L = 0.81$ and $L = 1.62$, the two reflections of the (111) orientation, (111)_{hex} and (222)_{hex}, respectively, are


Figure 12

(a) Comparison of XRD scans along the (00)-CTR for different deposition temperatures. (b) Comparison of L scans along the (22)_{cub}-CTR of Fe₃O₄(001) for different deposition temperatures. Here, the sharp outliers at $L = 1$ and $L = 2$ are due to diffuse scattering close to very intense substrate Bragg peaks being close to the measured CTRs.

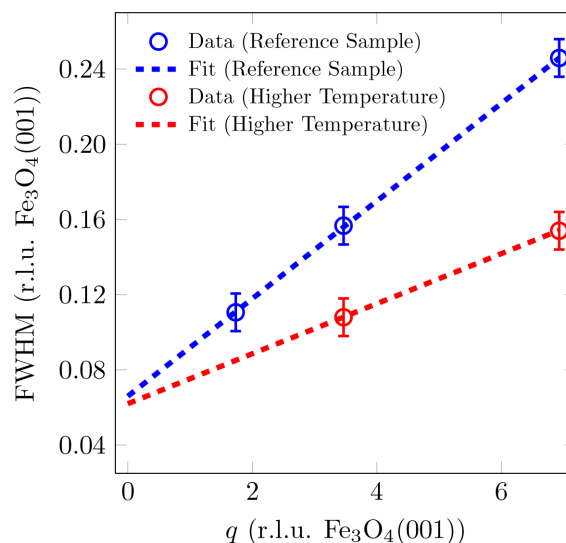

Figure 13

Schematic sketch of the grown film. The initial (111)-oriented Fe_3O_4 grows in 3D islands on the $\text{SrTiO}_3(001)$ substrate. Afterwards, the space between these islands is filled and covered by (001)-oriented Fe_3O_4 . Even though, for reasons of simplicity, the (111) orientation has been sketched here as simple islands on the substrate, it cannot be excluded that an additional thin layer of (111)-oriented Fe_3O_4 exists at the interface, meaning that this is a case of layer-plus-island growth (Stranski–Krastanov). This structure applies generally to all samples studied. Only the respective layer thicknesses and the proportion of (111) islands differ.

clearly recognisable. Accordingly, Fe_3O_4 is present in its (111) orientation in a significant proportion. The L scan along the $(22)_{\text{cub}}\text{-CTR}$ of $\text{Fe}_3\text{O}_4(001)$ also provides a comparable result [see Fig. 12(b)]. Here, too, all Fe_3O_4 reflections are sharper and more pronounced than for diffraction reflections obtained from the film deposited at lower temperature, especially $(31\bar{1})_{\text{hex}}^A$ belonging to the (111) orientation. The intensity ratio according to equation (2) results in a proportion of 9.7% for (111)-orientated Fe_3O_4 . Compared with the reference sample, this is a significant increase in the proportion of (111) orientation by a factor of 12.6 and confirms previous work that higher temperatures favour the (111) orientation of Fe_3O_4 on $\text{SrTiO}_3(001)$ (Takahashi *et al.*, 2012, 2014; Leung *et al.*, 2008).

The FWHM of $(004)_{\text{cub}}$ results in a crystalline film thickness of $d_{\text{cryst}} = 16.0$ (2) nm, which is in very good agreement with the deposited amount of Fe_3O_4 and is the highest value among the samples studied. This is probably due to the increased growth kinetics, which favour a better ordering of the layer. Since reflections of the (111) orientation of Fe_3O_4 can be seen in this sample on the $(00L)$ rod, these can also be used to determine the crystalline film thickness of the (111) orientation according to Scherrer [equation (1)]. This results in a crystalline film thickness of $d_{\text{cryst}} = 9.3$ (2) nm. Since both orientations of Fe_3O_4 together far exceed the amount of Fe_3O_4 deposited, the (111) orientation cannot be a continuous laminar intermediate layer. Rather, the (111)-oriented Fe_3O_4 must be present in the form of 3D islands, covered by the (001)-oriented Fe_3O_4 (*cf.* Fig. 13). In addition, the space between (111)-oriented 3D islands is filled by the (001)-oriented Fe_3O_4 film.

A comparable result can also be observed in the other samples. However, since the samples do not show any reflections of the (111) orientation on the (00)-CTR, $(31\bar{1})_{\text{hex}}^A$ must be used for this analysis. Since additional broadening due to mosaics cannot be excluded, only the minimum crystalline thickness that the (111) orientation must have can be estimated. Nevertheless, the minimum thickness for all samples is significantly higher than what would be expected for a laminar


Figure 14

FWHM analysis of (LLL) reflections of (001)-oriented Fe_3O_4 as a function of the scattering-vector magnitude q for different deposition temperatures. The FWHM of the peaks has been fitted with a linear function. As the data point on the $(111)_{\text{cub}}\text{-CTR}$ deviates significantly from the trend of the other data, it was not considered in the fit.

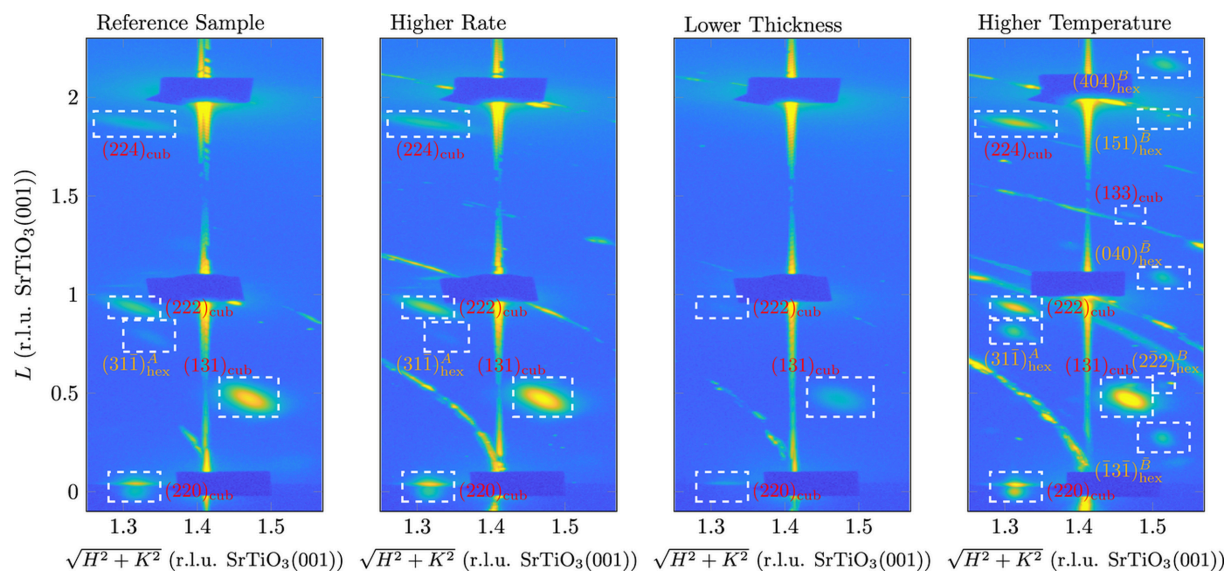
layer structure, *i.e.* yield \times deposited thickness, so that the island model is also applicable to the other samples.

In the same way as with the other samples, there is also a broadening of the $\text{Fe}_3\text{O}_4(001)$ reflections with q in the sample that was grown at a higher temperature (*cf.* Fig. 14). A fit here results in a lateral mosaic size with respect to the $[111]$ direction of $d_{\text{mosaic}} = 12.1$ (2) nm and a mosaic spread of $\Delta\sigma = 0.93$ (4) $^\circ$. The mosaic spread is the lowest of all four samples, which means that the mosaics are more ordered and tend to have a preferred direction, as well as the largest lateral extension.

3.5. HEXRD

To gain a deeper insight into the complete in-plane and out-of-plane structure of the ultrathin films, the samples were analysed *a posteriori* using HEXRD. Fig. 15 shows a section of the reciprocal-space map for the samples analysed near the $(22)_{\text{cub}}\text{-}$ and $(11)_{\text{STO}}\text{-CTR}$ s, where reflections are expected from both the (001) and (111) orientations of Fe_3O_4 .

As with the GIXRD in-plane map, only the more intense reflections are visible in the thin sample, even from the (001) orientation. In addition to the reflections of the $\text{Fe}_3\text{O}_4(001)$ orientation, $(31\bar{1})_{\text{hex}}^A$ on the $(22)_{\text{cub}}\text{-CTR}$ can be seen in the reference sample and the high-rate sample. In the high-temperature sample, on the other hand, all the expected reflections from the (111) orientation can be seen, except for the one that would be expected at approximately $\sqrt{H^2 + K^2} = 1.52$, $L = 1.3$ [r.l.u. $\text{SrTiO}_3(001)$]. However, this is $(3\bar{1}3)_{\text{hex}}^B$, which is significantly weaker than the other reflections due to the low form factor [*cf.* the $(133)_{\text{cub}}$ reflection to its left, which is barely visible even at the (001) orientation]. It is noticeable that the (111) orientation in the


Figure 15

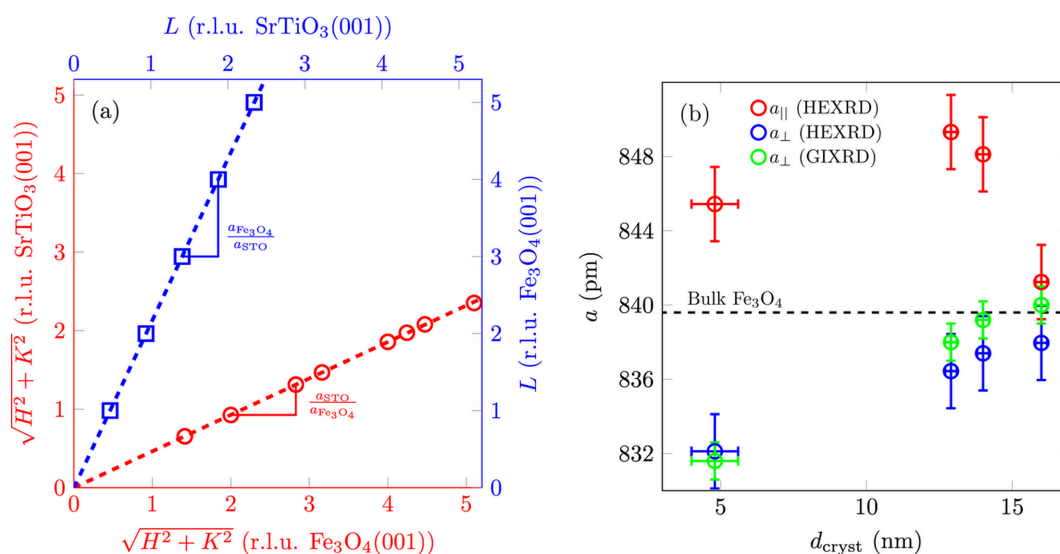
Sections of the recorded HEXRD reciprocal-space map for all four samples. The dark rectangles at the positions of the SrTiO₃ reflections are caused by beamstops used to protect the detector from the substrate's bright Bragg reflections.

reference sample and the high-rate sample is slightly laterally distorted or not fully relaxed, as $(31\bar{1})_{\text{hex}}^A$ is not fully aligned with the $(22)_{\text{cub}}$ -CTR, as expected for relaxed Fe₃O₄(001), but is slightly shifted towards the substrate reflection. This is not the case with the high-temperature sample, where the film is (almost) completely relaxed.

Analogously to the GIXRD in-plane map (*cf.* Section 3.1), the positions of the Fe₃O₄(111) reflections contradict the model proposed by Takahashi *et al.* (2012). Even though, in the case of the reference sample and the high-rate sample, the (111) orientation is not laterally relaxed, suggesting an initial

adaptation to the SrTiO₃(001) substrate's lattice, the lateral lattice vectors of the structure proposed by the Takahashi model would result in an expansion of 1.47% in the $[\bar{1}10]$ direction and a compression of 1.38% in the $[410]$ direction. Due to the projection of all lateral scattering vector components q_{\parallel} over a larger angle range of $\pm 90^\circ$, this would be apparent in the HEXRD out-of-plane reciprocal-space map as a double reflection at the position of $(31\bar{1})_{\text{hex}}^A$, which is not the case in the present measurements.

To obtain information about the vertical and lateral lattice constants a_{\perp} and a_{\parallel} for the possibly tetragonally distorted


Figure 16

(*a*) Determination of the vertical (blue) and lateral (red) lattice constants for the high-temperature sample. By plotting the fitted reflection positions against their nominal positions, the ratio of the lattice constants of the film and substrate can be obtained from the slope (dashed line). (*b*) Lateral and vertical lattice constants a_{\parallel} and a_{\perp} versus the crystalline layer thickness d_{cryst} of Fe₃O₄(001) determined from the fit in the HEXRD measurements. For comparison, the vertical lattice constants a_{\perp} determined from the difference of the reflections on the $(22)_{\text{cub}}$ -CTR are also plotted. The black dashed line denotes the value for bulk Fe₃O₄.

Fe₃O₄(001) film, the positions in reciprocal space of the visible reflections of the film were determined. Up to 15 Bragg peaks per sample were fitted with 2D Gaussians to obtain both their out-of-plane and their in-plane positions. If these positions in reciprocal lattice units of SrTiO₃ are then plotted against their nominal positions in lattice units of Fe₃O₄ and fitted with a linear function, the slope of this function corresponds to the ratio of the lattice constants between the substrate and the film [cf. Fig. 16(a)].

Fig. 16(b) shows the vertical and lateral lattice constants determined in the above method for the (001) orientation of Fe₃O₄, as well as the vertical lattice constant determined from the difference between the (222)_{cub} and (224)_{cub} reflections (cf. Section 3.1). The values for the vertical lattice constants determined using different methods agree very well within the range of errors, confirming the validity of both approaches. Within the limits of accuracy, all films except the thickest (high-temperature sample) are tetragonally distorted because their in-plane and out-of-plane lattice constants are different. For the vertical lattice constant, it can be seen that this increases with the crystalline film thickness d_{cryst} and approaches the value of bulk Fe₃O₄. This means that vertical compression is initially present and the film gradually relaxes as the thickness increases. Note that (except for the reference sample and the low-thickness sample) other parameters (rate, temperature) were also changed for each film thickness. For $d_{\text{cryst}} > 11.9$ (2) nm, the Fe₃O₄(001) film is fully relaxed in its vertical direction.

In the lateral direction, however, the film is initially expanded and relaxes (excluding the lower-thickness sample) as the film thickness increases, so that it is completely relaxed in the lateral direction as well for $d_{\text{cryst}} > 14.0$ (2) nm. However, since the doubled lattice constant of SrTiO₃(001) (3.905 Å) is 7.5% smaller than that of Fe₃O₄(001), lateral compression and vertical expansion are to be expected for pseudomorphic growth of ultrathin films and taking into account the theory of elastic strain. Nevertheless, this unusual strain with lateral expansion and vertical compression has already been observed in previous studies on thin films of Fe₃O₄, NiFe₂O₄ and CoFe₂O₄ on SrTiO₃(001), but so far there is no explanation for this behaviour (Gao *et al.*, 2009; Hoppe *et*

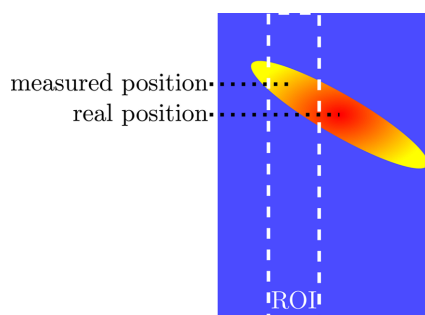


Figure 17
Schematic representation of how the position of a reflection located slightly outside the region of interest (ROI) is misinterpreted.

Table 1
Lateral and vertical layer distances c_{\parallel} and c_{\perp} of the (111) orientation of Fe₃O₄ determined from the fit in the HEXRD measurements.

For comparison, the vertical layer distances c_{\perp} determined from the measurement of the (22)_{cub}-CTR are also plotted. The layer distances of the low-thickness sample could not be determined due to the absence of the (311)_{hex}^A reflection.

	$c_{\parallel}^{\text{HEXRD}}$ (pm)	c_{\perp}^{HEXRD} (pm)	c_{\perp}^{GIXRD} (pm)
Reference sample	294.2 (7)	499.5 (12)	488.0 (5)
Higher rate	295.9 (7)	495.8 (12)	485.0 (5)
Higher temperature	297.8 (7)	480.4 (12)	481.0 (5)

et al., 2015; Moyer *et al.*, 2012; Thien *et al.*, 2020; Rodewald *et al.*, 2020; Kuschel *et al.*, 2017).

To determine the vertical and lateral layer distances c_{\perp} and c_{\parallel} of the (111) orientation, (311)_{hex}^A was used, as it was the only reflection that could be fitted for all samples except for that with lower thickness (cf. Table 1). Here, the vertical and lateral layer distances c_{\perp} and c_{\parallel} denote the layer distance of the (111) orientation of Fe₃O₄ in the [111] and [101] directions, respectively. For bulk Fe₃O₄, $c_{\perp} = 484.7$ pm and $c_{\parallel} = 296.8$ pm (Cornell & Schwertmann, 2003). Besides the high-temperature sample, the vertical layer distances determined from the HEXRD measurements and from the reflection position on the (22)_{cub}-CTR (GIXRD experiment) differ significantly from each other. This could be because, contrary to the assumption made in the GIXRD reciprocal-space maps (cf. Fig. 2), the (001) and (111) orientations fully overlap; in the reference sample and the high-rate sample (311)_{hex}^A does not coincide exactly with the (22)_{cub}-CTR (cf. Fig. 15). Due to its tilted orientation, its position in the L scan for the GIXRD experiment is overestimated (cf. Fig. 17).

In all three cases, the (111)-oriented films are highly strained compared with bulk Fe₃O₄ ($c_{\perp} = 484.7$ pm and $c_{\parallel} = 296.8$ pm). However, while the reference sample and high-rate sample are vertically expanded and laterally compressed, the high-temperature sample exhibits vertical compression and lateral expansion.

4. Summary

Ultrathin Fe₃O₄ films were grown on SrTiO₃(001) substrates under various growth conditions to investigate the influence of these parameters on the formation of the (111) orientation of Fe₃O₄. These films were then studied using *in situ* GIXRD and *ex situ* HEXRD, and both in-plane and out-of-plane reciprocal-space maps were recorded to obtain detailed structural information in both the lateral and vertical directions.

All samples grown exhibit high crystallinity, with the growth conditions and thus the kinetic parameters being crucial for the resulting structure. The lattice constants determined show a dependence on d_{cryst} (and other variations of the parameters for film preparation) and an atypical strain that cannot be explained by the standard theory of epitaxy. Moreover, all samples show mosaicity, which indicates misfit dislocations due to the high lattice mismatch between the film and

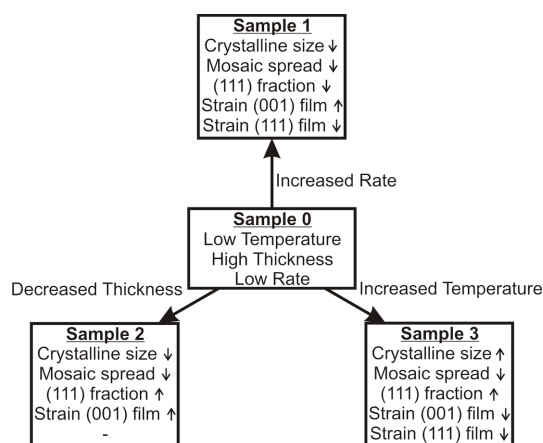


Figure 18

Schematic summary of the main structural changes in the samples studied by changing the growth parameters.

substrate. The main structural changes are summarized in Fig. 18.

In addition to the expected (001) orientation of Fe_3O_4 , the (111) orientation is present in all samples studied, forming four rotational domains. The formation of the (111) orientation is favoured by low deposition rates and, in particular, increased deposition temperatures. Investigations on the low-thickness sample show that the (111)-oriented film is predominantly formed at the beginning of film growth and then persists and coexists with the later formed (001) orientation. This (111) orientation forms 3D islands that are subsequently covered or filled by Fe_3O_4 with (001) orientation, which confirms previous investigations (Alexander *et al.*, 2025).

Acknowledgements

We acknowledge SOLEIL (Saint-Aubin, France) for the provision of beam time within the standard proposal 20191762 and we thank the synchrotron staff for assistance in using beamline SixS. We thank DESY (Hamburg, Germany), a member of the Helmholtz Association HGF, for the provision of experimental facilities. Parts of this research were carried out at PETRA III beamline P07 EH2. Beam time was allocated for proposal I-20230571. Furthermore, we acknowledge support by the PETRA III sample environment group. Open access funding enabled and organized by Projekt DEAL.

Funding information

Financial support from the Deutsche Forschungsgemeinschaft (DFG under Nos. KU2321/6-1, KU2321/6-2 and WO533/20-1) is gratefully acknowledged.

References

Alexander, A., Kleideiter, T., Pollenske, T., Ruwisch, K., Bertram, F. & Wollschläger, J. (2025). *Appl. Surf. Sci.* **684**, 161835.

- Bertram, F., Deiter, C., Hoefert, O., Schemme, T., Timmer, F., Suendorf, M., Zimmermann, B. & Wollschläger, J. (2012). *J. Phys. D Appl. Phys.* **45**, 395302.
- Bertram, F., Deiter, C., Pflaum, K., Suendorf, M., Otte, C. & Wollschläger, J. (2011). *J. Appl. Phys.* **110**, 102208.
- Bertram, F., Deiter, C., Schemme, T., Jentsch, S. & Wollschläger, J. (2013). *J. Appl. Phys.* **113**, 184103.
- Brown, P. J., Fox, A. G., Maslen, E. N., O'Keefe, M. A. & Willis, B. T. M. (2006). *International Tables for Crystallography*, Vol. C, *Mathematical, Physical and Chemical Tables*, edited by E. Prince, ch. 6.1, pp. 554–595. International Union of Crystallography.
- Celotto, S., Eerenstein, W. & Hibma, T. (2003). *Eur. Phys. J. B Condens. Matter* **36**, 271–279.
- Chang, C., Hu, Z., Klein, S., Liu, X., Sutarto, R., Tanaka, A., Cezar, J., Brookes, N., Lin, H.-J., Hsieh, H., Chen, C., Rata, A. & Tjeng, L. (2016). *Phys. Rev. X* **6**, 041011.
- Chen, Y. Z., Sun, J. R., Han, Y. N., Xie, X. Y., Shen, J., Rong, C. B., He, S. L. & Shen, B. G. (2008). *J. Appl. Phys.* **103**, 07D703.
- Cornell, R. M. & Schwertmann, U. (2003). *The Iron Oxides: Structure, Properties, Reactions, Occurrences and Uses*. Wiley-VCH Verlag.
- Dawiec, A., Garreau, Y., Bisou, J., Hustache, S., Kanoute, B., Picca, F., Renaud, G. & Coati, A. (2016). *J. Instrum.* **11**, P12018–P12018.
- Dynna, M., Vassent, J. L., Marty, A. & Gilles, B. (1996). *J. Appl. Phys.* **80**, 2650–2657.
- Gao, X. S., Bao, D. H., Birajdar, B., Habisreuther, T., Mattheis, R., Schubert, M. A., Alexe, M. & Hesse, D. (2009). *J. Phys. D Appl. Phys.* **42**, 175006.
- Goldbach, H. D. & Wollschläger, J. (2022). *J. Vac. Sci. Technol. A* **40**, 033403.
- Hamie, A., Dumont, Y., Popova, E., Fouchet, A., Warot-Fonrose, B., Gatel, C., Chikoidze, E., Scola, J., Berini, B. & Keller, N. (2012). *Thin Solid Films* **525**, 115–120.
- Hoffmann, A. & Bader, S. D. (2015). *Phys. Rev. Appl.* **4**, 047001.
- Hoppe, M., Döring, S., Gorgoi, M., Cramm, S. & Müller, M. (2015). *Phys. Rev. B* **91**, 054418.
- Hu, G. & Suzuki, Y. (2002). *Phys. Rev. Lett.* **89**, 276601.
- Jordan, K., Cazacu, A., Manai, G., Ceballos, S. F., Murphy, S. & Shvets, I. V. (2006). *Phys. Rev. B* **74**, 085416.
- Kado, T. (2008). *Appl. Phys. Lett.* **92**, 092502.
- Kale, S., Bhagat, S. M., Lofland, S. E., Scabarozzi, T., Ogale, S. B., Orozco, A., Shinde, S. R., Venkatesan, T., Hannoyer, B., Mercey, B. & Prellier, W. (2001). *Phys. Rev. B* **64**, 205413.
- Kim-Ngan, N.-T., Balogh, A., Meyer, J., Brötz, J., Zajac, M., Ślęzak, T. & Korecki, J. (2009). *Surf. Sci.* **603**, 1175–1181.
- Kuschel, O., Buß, R., Spiess, W., Schemme, T., Wöllermann, J., Balinski, K., N'Diaye, A. T., Kuschel, T., Wollschläger, J. & Kuepper, K. (2016). *Phys. Rev. B* **94**, 094423.
- Kuschel, O., Spiess, W., Schemme, T., Rubio-Zuazo, J., Kuepper, K. & Wollschläger, J. (2017). *Appl. Phys. Lett.* **111**, 041902.
- Leung, G. W., Vickers, M. E., Yu, R. & Blamire, M. G. (2008). *J. Cryst. Growth* **310**, 5282–5286.
- Liu, X. H., Liu, W. & Zhang, Z. D. (2017). *Phys. Rev. B* **96**, 094405.
- Margulies, D. T., Parker, F. T., Rudee, M. L., Spada, F. E., Chapman, J. N., Aitchison, P. R. & Berkowitz, A. E. (1997). *Phys. Rev. Lett.* **79**, 5162–5165.
- Marnitz, L., Rott, K., Niehörster, S., Klewe, C., Meier, D., Fabretti, S., Witzkiok, M., Krampf, A., Kuschel, O., Schemme, T., Kuepper, K., Wollschläger, J., Thomas, A., Reiss, G. & Kuschel, T. (2015). *AIP Advances* **5**, 047103.
- Mishra, R. K. & Thomas, G. (1977). *J. Appl. Phys.* **48**, 4576–4580.
- Monti, M., Sanz, M., Oujja, M., Rebollar, E., Castillejo, M., Pedrosa, F. J., Bollero, A., Camarero, J., Cuñado, J. L. F., Nemes, N. M., Mompean, F. J., Garcia-Hernández, M., Nie, S., McCarty, K. F., N'Diaye, A. T., Chen, G., Schmid, A. K., Marco, J. F. & de la Figuera, J. (2013). *J. Appl. Phys.* **114**, 223902.
- Moussy, J.-B. (2013). *J. Phys. D Appl. Phys.* **46**, 143001.
- Moyer, J. A., Kumah, D. P., Vaz, C. A. F., Arena, D. A. & Henrich, V. E. (2012). *Appl. Phys. Lett.* **101**, 021907.

- Pohlmann, T., Hoppe, M., Thien, J., Dey, A. B., Alexander, A., Ruwisch, K., Gutowski, O., Röh, J., Gloskovskii, A., Schlueter, C., Küpper, K., Wollschläger, J. & Bertram, F. (2022). *Phys. Rev. B* **105**, 045412.
- Ramos, R., Anadón, A., Lucas, I., Uchida, K., Algarabel, P. A., Morellón, L., Aguirre, M. H., Saitoh, E. & Ibarra, M. R. (2016). *APL Mater.* **4**, 104802.
- Ramos, R., Kikkawa, T., Uchida, K., Adachi, H., Lucas, I., Aguirre, M. H., Algarabel, P., Morellón, L., Maekawa, S., Saitoh, E. & Ibarra, M. R. (2013). *Appl. Phys. Lett.* **102**, 072413.
- Rodewald, J., Thien, J., Pohlmann, T., Hoppe, M., Timmer, F., Bertram, F., Kuepper, K. & Wollschläger, J. (2019). *Phys. Rev. B* **100**, 155418.
- Rodewald, J., Thien, J., Ruwisch, K., Bertram, F., Kuepper, K. & Wollschläger, J. (2020). *Phys. Rev. Mater.* **4**, 064404.
- Rubio-Zuazo, J., Onandia, L., Salas-Colera, E., Muñoz-Noval, A. & Castro, G. R. (2015). *J. Phys. Chem. C* **119**, 1108–1112.
- Santos-Carballal, D., Roldan, A., Grau-Crespo, R. & de Leeuw, N. H. (2014). *Phys. Chem. Chem. Phys.* **16**, 21082–21097.
- Scherrer, P. (1918). *Bestimmung der inneren Struktur und der Größe von Kolloidteilchen mittels Röntgenstrahlen*, pp. 98–100. Berlin: Weidmannsche Buchhandlung.
- Seneor, P., Fert, A., Maurice, J.-L., Montaigne, F., Petroff, F. & Vaurès, A. (1999). *Appl. Phys. Lett.* **74**, 4017–4019.
- Takahashi, R., Misumi, H. & Lippmaa, M. (2012). *Cryst. Growth Des.* **12**, 2679–2683.
- Takahashi, R., Misumi, H. & Lippmaa, M. (2014). *J. Appl. Phys.* **116**, 033918.
- Thien, J., Bahlmann, J., Alexander, A., Hoppe, M., Pohlmann, T., Ruwisch, K., Meyer, C., Bertram, F., Küpper, K. & Wollschläger, J. (2020). *J. Phys. Chem. C* **124**, 23895–23904.
- Tobin, J. G., Morton, S. A., Yu, S. W., Waddill, G. D., Schuller, I. K. & Chambers, S. A. (2007). *J. Phys. Condens. Matter* **19**, 315218.
- Uchida, K., Adachi, H., Kikkawa, T., Kirihara, A., Ishida, M., Yorozu, S., Maekawa, S. & Saitoh, E. (2016). *Proc. IEEE* **104**, 1946–1973.
- van der Zaag, P. J., Bloemen, P. J. H., Gaines, J. M., Wolf, R. M., van der Heijden, P. A. A., van de Veerdonk, R. J. M. & de Jonge, W. J. M. (2000). *J. Magn. Magn. Mater.* **211**, 301–308.
- Vassent, J. L., Dynna, M., Marty, A., Gilles, B. & Patrat, G. (1996). *J. Appl. Phys.* **80**, 5727–5735.
- Wada, E., Watanabe, K., Shirahata, Y., Itoh, M., Yamaguchi, M. & Taniyama, T. (2010). *Appl. Phys. Lett.* **96**, 102510.
- Wollschläger, J. (2018). *Encyclopedia of Interfacial Chemistry*, Vol. 3.1, pp. 284–296. Elsevier.
- Wollschläger, J., Erdös, D., Goldbach, H., Höpken, R. & Schröder, K. M. (2001). *Thin Solid Films* **400**, 1–8.
- Yu, X., Huo, C.-F., Li, Y.-W., Wang, J. & Jiao, H. (2012). *Surf. Sci.* **606**, 872–879.
- Zhang, Z. & Satpathy, S. (1991). *Phys. Rev. B* **44**, 13319–13331.